Focusing of elastic waves for microseismic imaging

Johannes Douma and Roel Snieder
Center for Wave Phenomena, Colorado School of Mines, Golden, Colorado 80401

ABSTRACT
Microseismic events generate compressive waves and shear waves which can be recorded at receivers. We present a theory that shows how elastic P and S waves separately backpropagate to the original source location. These refocused P and S wavefields are free of singularities. We also demonstrate a technique that enhances the ability to image the spatial focus for each wave type using elastic waves. The improved spatial focus obtained is achieved in a velocity model for which the interface boundaries are approximate but where the mean slowness is correct. Deconvolution designs a signal to be rebroadcasted from the receivers, using only the waves recorded at each receiver, such that the wavefield has an optimal temporal focus at the source location. We demonstrate theoretically and numerically that improved temporal focusing of elastic waves leads to improved spatial focusing for each wave type. This proposed technique only involves a simple preprocessing step to the recorded data and its cost is hence negligible compared to the total cost of microseismic imaging.

Key words: Deconvolution, Signal Focusing, Image processing, Fractures and faults, Computational seismology, and Earthquake source observations

1 INTRODUCTION

Due to hydraulic fracturing becoming a common practice for unconventional gas and oil fields, there has been an increased interest into the study of microseismic events. Clusters of microseismic events delineate faults and the formation of fractures, and can indicate new or reactivating regions of failure. These microseismic events can be generated naturally or as a result of hydraulic stimulation (Duncan, 2005; Kendall et al., 2011). Therefore, the petroleum industry desires to develop more accurate ways of locating, and monitoring microseismic events to potentially improve their relationship to production and completion data (Foulger and Julian, 2012).

A common processing method to locate microseismic events or earthquakes is based on picking arrival times of the acoustic and shear waves. This process, however, is difficult to do accurately when significant noise is present in the data (Bose et al., 2009; Bancroft et al., 2010; Kummerow, 2010; Song et al., 2010; Hayles et al., 2011). An alternative approach, which requires less user interaction and allows for more accuracy, is using time reversal to image the focus of the microseismic events or earthquakes at the source location (McMechan et al., 1985; Larmat et al., 2006, 2010; Lu, 2008; Steiner et al., 2008; Lu et al., 2008; Artman et al., 2010). In this imaging approach, one uses time reversal to focus the recorded signal at the source location in both time and space. The advantage of time reversal is that it does not require picking of arrival times which is important when dealing with noisy data.

If one would time reverse the waves at every point in space, the wavefield will focus onto the original source location. If, however, the wavefield is sampled at only a limited number of locations, then it is not obvious that time reversal is the optimal way to focus energy on the original source. Much research has been carried out on focusing sparsely sampled wavefields (Parvulescu, 1961; Fink, 1997; Roux and Fink, 2000; Tanter et al., 2000, 2001; Aubry et al., 2001; Bertaix et al., 2004; Jonsson et al., 2004; Montaldo et al., 2004; Vignon et al., 2006; Larmat et al., 2010; Gallot et al., 2011). In this paper, we explore a simple extension to time reversal, based on deconvolution, as previously derived by Ulrich et al. (2013). We have shown earlier that deconvolution improves the locating of microseismic events in an acoustic medium (Douma et al., 2013). We now demonstrate deconvolution's ability to improve the imaging of a microseismic event in an elastic medium. This method is a robust, though simplified, version of the inverse filter (Tanter et al., 2000, 2001; Gallot et al., 2011). It calcu-

lates a signal to be rebroadcast from the receiver such that the output at the focal location becomes an approximate delta function $\delta(t)$ and uses only the recorded signals at each receiver.

As with all imaging methods, reverse time imaging is unable to locate the microseismic event to a point location when the velocity model used for the backpropagation differs from the true velocity model, or when the aperture is limited; it causes the spatial image to defocus. In the numerical example used for this paper, the aperture used is not perfect, thus, the wavefield is not know at every point in both time and space. Additionally, we complicate our model by back-propagating our wavefields not through the correct velocity model but through a smoothed version of the velocity model.

In this paper, we first derive a relationship between the temporal focus and the incoming wave for an elastic medium. The theory is used to show that improved temporal focusing leads to improved spatial focusing for each wave type due to different sources (explosive, point force, and double couple). We then show a numerical example in which a horizontal point force excites elastic waves.

2 THEORY

In this section, we show that improved temporal focusing leads to improved spatial focusing for both P- and S-waves. We first consider a homogeneous elastic medium where either P, SV, or SH waves are incident on a focal point. According to expression (8.13) of Aki and Richards (2002), the elastic wavefield can be expressed as

$$\mathbf{u}(r,\theta,\varphi) = \sum_{lm} (U_l(r)\mathbf{R}_l^m(\theta,\varphi) + V_l(r)\mathbf{S}_l^m(\theta,\varphi) + W_l(r)\mathbf{T}_l^m(\theta,\varphi)) \,. \tag{1}$$

The vector spherical harmonics in equation 1 are given by

$$\mathbf{R}_l^m(\theta,\varphi) = Y_{lm}(\theta,\varphi)\hat{\mathbf{r}} \qquad (\mathrm{P}-\mathrm{waves}) \,, \tag{2}$$

$$\mathbf{S}_l^m(\theta,\varphi) = \frac{1}{\sqrt{l(l+1)}}\left(\frac{\partial Y_{lm}(\theta,\varphi)}{\partial\theta}\hat{\theta} + \frac{1}{\sin\theta}\frac{\partial Y_{lm}(\theta,\varphi)}{\partial\varphi}\hat{\varphi}\right) \quad (\mathrm{SV}-\mathrm{waves}) \,, \tag{3}$$

$$\mathbf{T}_l^m(\theta,\varphi) = \frac{1}{\sqrt{l(l+1)}}\left(\frac{1}{\sin\theta}\frac{\partial Y_{lm}(\theta,\varphi)}{\partial\varphi}\hat{\theta} - \frac{\partial Y_{lm}(\theta,\varphi)}{\partial\theta}\hat{\varphi}\right) \quad (\mathrm{SH}-\mathrm{waves}) \,, \tag{4}$$

where $Y_{lm}(\theta,\varphi)$ denote the spherical harmonics. The radial functions $U_l(r)$, $V_l(r)$ and $W_l(r)$ are spherical Bessel functions or spherical Hankel functions which satisfy equation (8.6) of Aki and Richards (2002).

We consider the case of an incoming wave that, at a large distance from the focal point $\vec{r} = 0$, is given by $f_l(t + r/c)/r$. We study the properties of this incoming wave at the focus for every angular degree l separately. For a perfect aperture, the angular degree l describes an explosive source when $l = 0$, a point force when $l = 1$, and a double-couple source when $l = 2$. Since there is no source at the location $\vec{r} = 0$, the solution is finite and is therefore given by spherical Hankel functions j_l :

$$U_l(r) \propto j_l(kr) \qquad \text{where} \qquad k = \omega/\alpha \,, \tag{5}$$

with α representing the P-wave velocity, and

$$V_l(r) \qquad \text{and} \qquad W_l(r) \propto j_l(kr) \qquad \text{with} \qquad k = \omega/\beta \,, \tag{6}$$

where β the S-wave velocity. Thus, the radial variation of the wavefield is proportional to $j_l(kr)$, with k the wavenumber of the wave type under consideration. In the following, we study wavefields with radial dependence $j_l(kr)$ and denote the wavenumber as

$$k = \omega/c \,, \tag{7}$$

where c is the appropriate wave velocity (α or β depending on the wave type). It is understood that the total wavefield follows by multiplying with the appropriate vector spherical harmonic as given in expressions (2)-(4). The radial dependence of the wavefield in the frequency domain, therefore, is given by

$$U_l(r,\omega) = A_l(\omega) j_l(kr) \,, \tag{8}$$

where $A_l(\omega)$ is a Fourier coefficient.

Using the Fourier convention $f(t) = \int F(\omega) e^{-i\omega t} d\omega$, the wavefield in the time domain is given by

$$u_l(r,t) = \int A_l(\omega) j_l(kr) e^{-i\omega t} d\omega \,. \tag{9}$$

The waves impinging on the focus are determined by the incoming waves. For large radius r, the incoming waves can be written as

$$u_l^{inc}(r,t) = \frac{f_l(t + r/c)}{r} \qquad \text{as} \qquad r \to \infty \,. \tag{10}$$

We show in the appendix that the total wavefield is given for all values of r by,

$$u_l(r,t) = (-i)^l \, \frac{2}{c} \int (-i\omega) F_l(\omega) j_l(kr) e^{-i\omega t} d\omega \ , \quad (11)$$

where $F_l(\omega)$ is the temporal Fourier transform of $f_l(t)$.

Because our derivation involves repeated differentiations and integrations, we employ the following notation:

$$f_l^{(n)}(t) \equiv \frac{d^n f_l(t)}{dt^n} \ . \quad (12)$$

For negative values of n, this notation implies integrating $f_l(t)$ n-times. In the frequency domain, the notation (12) translates into

$$F_l^{(n)}(\omega) \equiv (-i\omega)^n F_l(\omega) \ . \quad (13)$$

Next, we relate the total wavefield $u_l(r,t)$ to the spherical Bessel function of order 0 which makes it possible to evaluate the Fourier integral in equation (11) analytically. This derivation, found in the appendix, gives:

$$u_l(r,t) = c^l r^l \left(\frac{1}{r} \frac{d}{dr} \right)^l \left(\frac{f_l^{(-l)}(t+r/c) - f_l^{(-l)}(t-r/c)}{r} \right) \ . \quad (14)$$

This expression shows an explicit relationship between the total wavefield $u_l(r,t)$ for all values of r, and the incident wave, $f_l(t+r/c)/r$ at a great distance $r \to \infty$. Note that using the notation of equations (12)-(13), the incoming wave is integrated l times in the factor $f_l^{(-l)}(t \pm r/c)$, and that the differential operator $(1/r)(d/dr)$ acts l times as well. The term $f_l^{(-l)}(t+r/c)$ is the wave that converges on the focal point, while $f_l^{(-l)}(t-r/c)$ gives the outgoing wave that radiates from the focus after the incoming waves has passed through that point. The incident wave $f_l(t+r/c)$ and the outgoing wave $f_l(t-r/c)$ have opposite sign because the focus is a caustic in two angular directions, hence the Maslow index increases by two, which corresponds to a sign change (Chapman, 2004).

We now demonstrate how we can use the expression for the wavefield near the focal point to demonstrate that improved temporal focusing leads to improved spatial focusing. The spatial focus $R_l(r)$ is defined as the wavefield at time $t = 0$. It follows from expression (14) that the spatial focus is given by:

$$R_l(r) \equiv u_l(r, t=0) = c^l r^l \left(\frac{1}{r} \frac{d}{dr} \right)^l \left(\frac{f_l^{(-l)}(r/c) - f_l^{(-l)}(-r/c)}{r} \right) \ . \quad (15)$$

This expression gives the spatial focus in terms of the incoming wave.

One might be tempted to define the temporal focus as $u_l(r=0,t)$. This field, according to expression (9), is proportional to $j_l(kr)$ in the frequency domain. The zeroth order Bessel function $j_0(kr)$ is nonzero for $r = 0$, but $j_l(kr = 0) = 0$ for $l \geq 1$ (Arfken and Weber, 2001). This means that for $l \geq 1$, the wavefield vanishes at the focal point. Physically, this is due to the fact that for $l \geq 1$, the focal point ($r = 0$) is located at the intersection of nodal lines. Since $U_l(r=0,t)$ vanishes at $r = 0$ for $l \geq 1$, this quantity is not a useful diagnostic of the temporal focus. To remedy this, we define the temporal focus instead as

$$T_l(t) \equiv \frac{d^l}{dr^l} u_l(r=0,t) \ . \quad (16)$$

As shown in the appendix, the l-th derivative of $j_l(kr)$ is finite and nonzero for $r = 0$. We derive in the appendix the following relation between the temporal focus and the incoming waves,

$$T_l(t) = \frac{2 b_l}{c^{l+1}} f_l^{(l+1)}(t) \ , \quad (17)$$

where b_l is given by

$$b_l = \frac{2^l (l!)^2}{(2l+1)!} . \quad (18)$$

Specifically,

$$b_0 = 1 \ , \ \ b_1 = 1/3 \ , \ \ b_2 = 2/15.$$

According to equation (17), the temporal focus thus is proportional to the $(l+1)$-th time derivative of the incoming wave. Of these $(l+1)$ derivatives, given by equation (17), l are due to the derivatives in definition (16). One time derivate is due to the fact that (14) contains the combination $\left(f_l(t+r/c) - f_l(t-r/c)\right)/r$. Using a Taylor expansion and taking the limit $r \to 0$, gives

$$\lim_{r \to 0} \frac{f_l(t+r/c) - f_l(t-r/c)}{r} = \lim_{r \to 0} \frac{2(r/c) f_l^{'}(t)}{r} = \frac{2}{c} f_l^{'}(t).$$

This explains an additional time derivative in expression (17).

3 SPATIAL AND TEMPORAL FOCUS FOR EACH ANGULAR COMPONENT

The spatial and temporal focus defined by expressions (15) and (17) both relate to the incoming waves and can be combined to explicitly relate the spatial and temporal focus:

$$R_l(r) = \frac{c^{2l+1}}{2b_l} r^l \left(\frac{1}{r}\frac{d}{dr}\right)^l \left(\frac{T_l^{(-2l-1)}(r/c) - T_l^{(-2l-1)}(-r/c)}{r}\right) . \tag{19}$$

Equation (19) is the main result of the theory. Although the relation (19) between the spatial and temporal focus is complicated, it does show that good temporal focusing implies good spatial focusing. Good temporal focusing implies that $T_l(t)$ is strongly peaked near $t = 0$, i.e. that $T_l(t)$ only differs appreciably from zero for a small range of time values $-t_f < t < t_f$, where t_f is the half width of the temporal focus. Expression (19) implies that the spatial focus differs appreciably from zero for values of r that satisfy $0 \le r < ct_f$ (radius is always positive). A good temporal focus (small t_f) thus implies a good spatial focus.

The spatial and temporal focus, and their relationship defined by equations (15), (17), and (19) all depend on the order l. In this section, we show the explicit forms of these expressions for the case $l = 0$, $l = 1$, and $l = 2$. These cases are relevant for an explosive source ($l = 0$), point force ($l = 1$) and double-couple source ($l = 2$) if the aperture would be perfect. For $l = 0$, equations (15), (17), and (19) become respectively,

$$R_0(r) = \left(\frac{f_0(r/c) - f_0(-r/c)}{r}\right) , \tag{20}$$

$$T_0(t) = \frac{2}{c} f_0^{(1)}(t) , \tag{21}$$

$$R_0(r) = \frac{c}{2}\left(\frac{T_0^{(-1)}(r/c) - T_0^{(-1)}(-r/c)}{r}\right) . \tag{22}$$

Equations (20),(21), and (22) are the same as shown in the previous derivation of Ulrich et al. (2013) which dealt with an explosive source in an acoustic medium where the temporal focus is the time derivative of the incoming wave.

We now continue the derivation for $R(r)$ due to a point force ($l = 1$) and double-couple ($l = 2$). For $l = 1$, equations (15), (17), and (19) become respectively,

$$\begin{aligned} R_1(r) = {} & \frac{1}{r}\left(f_1(r/c) + f_1(-r/c)\right) \\ & - \frac{c}{r^2}\left(f_1^{(-1)}(r/c) - f_1^{(-1)}(-r/c)\right) , \end{aligned} \tag{23}$$

$$T_1(t) = \frac{3}{2c^2} f_1^{(2)}(t) , \tag{24}$$

$$\begin{aligned} R_1(r) = {} & \frac{2c^2}{3}\frac{1}{r}\left(T_1^{(-2)}(r/c) + T_1^{(-2)}(-r/c)\right) \\ & - \frac{2c^3}{3}\frac{1}{r^2}\left(T_1^{(-3)}(r/c) - T_1^{(-3)}(-r/c)\right) . \end{aligned} \tag{25}$$

It may appear that equation (23) is singular at $r = 0$. Even though each of the two terms in this expression diverge as $r \to 0$, the singularities cancel. This can be verified by writing $f_1(r/c) = a_0 + O(r)$. Integrating this once gives $f_1^{(-1)}(r/c) = a_0(r/c) + O(r^2)$. Inserting this into equation (23) gives

$$R_1(r) = \frac{1}{r}\left(2a_0 + O(r)\right) - \frac{c}{r^2}\left(2a_0(r/c) + O(r^2)\right) . \tag{26}$$

The terms proportional to a_0, which caused each of the individual terms in expression (23) to be singular, cancel out. The remainder of equation (26) is finite as $r \to 0$.

For $l = 2$, equations (15), (17), and (19) become respectively,

$$\begin{aligned} R_2(r) = {} & \frac{1}{r}\left(f_2(r/c) - f_2(-r/c)\right) \\ & - \frac{3c}{r^2}\left(f_2^{(-1)}(r/c) + f_2^{(-1)}(-r/c)\right) \\ & + \frac{3c^2}{r^3}\left(f_2^{(-2)}(r/c) - f_2^{(-2)}(-r/c)\right) . \end{aligned} \tag{27}$$

$$T_2(t) = \frac{4}{15c^3} f_2^{(3)}(t) , \tag{28}$$

$$\begin{aligned} R_2(r) = {} & \frac{15c^3}{4}\frac{1}{r}\left(T_2^{(-3)}(r/c) - T_2^{(-3)}(-r/c)\right) \\ & - \frac{45c^4}{4}\frac{1}{r^2}\left(T_l^{(-4)}(r/c) + T_l^{(-4)}(-r/c)\right) \\ & + \frac{45c^5}{4}\frac{1}{r^3}\left(T_l^{(-5)}(r/c) - T_l^{(-5)}(-r/c)\right) . \end{aligned} \tag{29}$$

The wavefields computed are finite at the focal point $r = 0$ when one refocuses either P or S-waves. In contrast, when P and S-waves are excited by a point force, the P-wave component and the S-wave component behave as $1/r^3$ as $r \to 0$, hence the P-wave and S-wave separately have a non-integrable singularity at $r = 0$, while their sum has an $1/r$ singularity Wu (1985), which is integrable. The refocused wavefields don't display this behavior because these fields are source-free at $r = 0$, and therefore the wavefield is finite. Therefore, the P and S-waves can be refocused separately without causing singularities, and the treatment given here is applicable to P, SV, and SH waves separately.

The expressions above must be multiplied with the appropriate vector spherical harmonic (2)-(4) to obtain

the full focused wavefield. For each wave type, a different spherical harmonic must be multiplied to characterize the wavefield. Additionally, in equations (2)-(4), the vector spherical harmonics are summed over the angular order l and degree m which captures the imprint of the source properties on each wave type. Therefore, each wave has its own dependence on the angles and on space and time.

If one were to use one component of the motion, such as the x-component, the source properties for the different wave types are superposed on each other. Since for a fixed source mechanism the radiation pattern of P and S waves are different, the focused wavefields do not provide clear information about the source mechanism. In order to avoid mixing of P- and S- radiated waves, one must decompose the wavefield using the divergence and curl in order to investigate the focus of each wave type (P and S) separately.

If one does not have a perfect aperture, a blurred focus will occur, and the focus can not be characterized by one angular degree l but by the superposition of different angular degrees l. This is important to describe the spatial focus achieved in our numerical modeling.

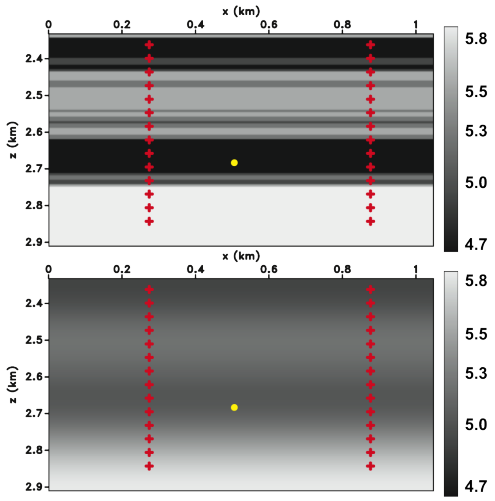

Figure 1. P-wave velocity models of the numerical experiment with units of km/s. Top panel indicates the correct velocity model and represents the velocity model used to propagate the source wavefield through the medium. Bottom panel indicates the smoothed velocity model with correct mean slowness. This model is used for back-propagation of the time reversed signal and optimized inverse signal. The plus symbols represent the receivers, the circular dot represents the source. The S-wave velocity was the same but had velocities values equal to half of the P-wave velocity.

4 NUMERICAL EXAMPLE

We illustrate the theory with a numerical example. We use the velocity model shown in the top panel of Figure 1 to propagate the source wavefield to the receivers. The model consists of horizontally continuous layers whose P-wave velocities range from approximately 4.7 km/s to 5.9 km/s and S-wave velocities range from approximately 2.3 km/s to 2.9 km/s. In practice, one does not know the true velocity model. For this reason, we used the smoothed velocity model, shown in the bottom panel of Figure 1, for the back-propagation. The velocity model is smoothed by using a two-dimensional triangle smoothing of the slowness with a smoothing radius of .185 km in the x and z directions (Fomel, 2007). This smoothed velocity model has the same mean slowness as the correct velocity model.

We use a horizontal point force located at (x, z) = (0.51 km, 2.68 km). The source is characterized by Ricker wavelet with dominant frequency of 100 Hz. There are 56 receivers distributed over 2 vertical boreholes in our model. The x-locations of the receiver boreholes are 0.74 km and 0.88 km respectively. The receivers range from a depth of 2.36 km to 2.86 km with a spacing of 18.5 m.

5 HORIZONTAL POINT FORCE

This section describes the numerical modeling that demonstrates that improved temporal focusing leads to improved spatial focusing for each wave type. We first model the wavefield due to a horizontal point force excitation at the source location. The horizontal and vertical displacements of the wavefield are then recorded at each receiver. Afterwards, we apply either time reversal or deconvolution to the recorded signals to generate the wavefields which are back-propagated.

We use the time reversed or deconvolved signals to excite waves that backpropagate through the smoothed velocity model, using the following forces acting at each of the receiver locations,

$$\vec{F}_{TimeReverse} = (U_x(-t), U_z(-t))), \tag{30}$$

$$\vec{F}_{Deconv} = (U_x^{Inverse}(t), U_z^{inverse}(t)) \, . \tag{31}$$

Here, $\vec{F}_{TimeReverse}$ and $\vec{F}_{Deconv}$ are the source functions for time reversal and deconvolution respectively, and $U_x(t)$ and $U_z(t)$ are the recorded signals. The inverse signal of a time series $g(t)$ is defined as,

$$g^{inverse}(t) \star g(t) = \delta(t). \tag{32}$$

where $\star$ denotes convolution. In order to solve for $g^{inverse}(t)$ and avoid instability for $g^{inverse}(\omega)$ when $g(\omega) = 0$, we have apply a water level regularization. Thus,

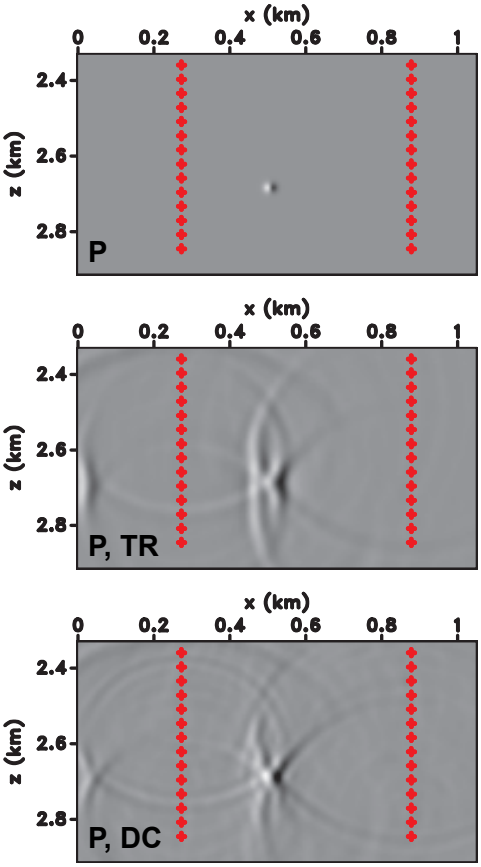

Figure 2. Decomposed P wavefield at time of focus due to horizontal point force. Top panel is P-wave just after the horizontal point force is emitted. Middle panel indicates the result of injecting the time reversed signal back into the smoothed velocity model from the receiver locations. Bottom panel shows result of injecting the inverse signal calculated using deconvolution back into the smoothed velocity model from the receiver locations.

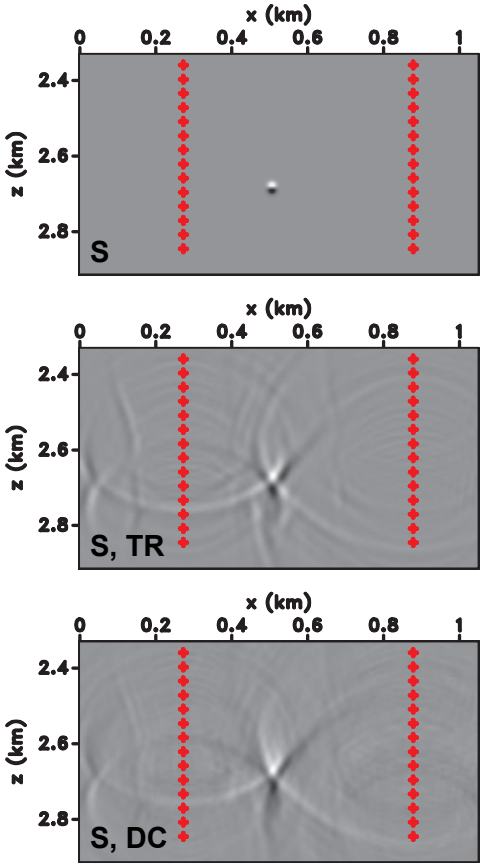

Figure 3. Decomposed S wavefield at time of focus due to horizontal point force. Top panel is S-wave just after the horizontal point force is emitted. Middle panel indicates the result of injecting the time reversed signal back into the smoothed velocity model from the receiver locations. Bottom panel shows result of injecting the inverse signal calculated using deconvolution back into the smoothed velocity model from the receiver locations.

$$g^{inverse}(\omega) = \frac{1}{g(\omega)} \Rightarrow \frac{g^*(\omega)}{|g^*(\omega)|^2 + \epsilon}. \qquad (33)$$

The derivation and explanation of these two methods are discussed in more detail by Douma et al. (2013).

After backpropagation, the wavefield is decomposed into P and S components for a crucial reason. We demonstrated in the theory section that improved temporal focusing leads to improved spatial focusing for each wave type. We do not consider the focus for the vertical or horizontal displacements. Rather, we use the displacement components to calculate the P and S wavefields using divergence and curl, respectively. This allows us to retrieve the P and S waves that have backpropagated from the sources. For each wave type, our theory predicts that an improved temporal focusing leads to improved spatial focusing.

We first model the wavefield due to a horizontal point force excitation at the source location. The top panel of Figures 2 and 3 show the P and S wavefields' radiation pattern just after the horizontal point force is emitted and represent a pure angular degree $l = 1$. In perfect source imaging, we would reconstruct these radiation patterns. However, our aperature is not perfect and we backpropagate through a smoother version of the velocity model. Thus, we do not expect to be able to reconstruct these radiation patterns perfectly.

In order to show that deconvolution generates an improved spatial focus, we first demonstrate that deconvolution enhances the temporal focus. Thus, we calculate the temporal focusing for the P and S component as a result of deconvolution (equation (31)) compared with time reversal (equation (30)). We defined the temporal focusing in equation (16) as the l-th derivative of the incoming wavefield. This is necessary because the

wavefield is zero at our source location due of nodal lines. In order to demonstrate improved temporal focusing for a horizontal point force, we take the derivative of the P wavefield in the x-direction and the derivative of the S-wavefield in the z-direction because these derivatives are the radial derivatives perpendicular to the nodal lines for each wave type. We change the direction of the derivative because the radiation pattern of the P-wave due to a horizontal point force is a dipole in the x-direction while the S-wave radiation has a dipole pattern oriented in the z-direction (Aki and Richards, 2002). This is visible in the top panel of Figures 2 and 3, which show the radiation patterns of the P and S wavefields just after the source has acted. We calculate the derivatives as defined above to show the temporal focus for the P and S wave at the source location. Comparing Figure 4(a) to 4(b), one can clearly note that deconvolution has significantly improved the temporal focusing compared to time reversal for the P-wave. In contrast, Figures 4(c) and (d) show that both time reversal and deconvolution produce a similar temporal focus for the S wave. Because improved temporal focusing implies better spatial focusing, see equation (26), one would expect to see an improved spatial focus improved for the P-wave using deconvolution compared to using time reversal. Additionally, we don't expect the S-wave's spatial focus to improve using deconvolution because the temporal focus did not improve.

After having demonstrated that deconvolution improved the temporal focusing for the P wave, we compare the spatial focus generated by deconvolution and time reversal for each wave type. The backpropagated wavefields at $t = 0$ for the two methods are shown in the middle and bottom panels of Figure 2 and 3. The middle panel of Figure 2 represents the spatial focus of the P wave using time reversal whereas the bottom panel shows the spatial focus of the P wave using time-reversal. Figure 2 shows that deconvolution drastically improves the spatial focus compared to deconvolution. Figure 3 does not show a clear improvement of spatial focusing between time reversal (middle panel) and deconvolution (bottom panel) for the S component. This was expected due to deconvolution and time reversal producing similar temporal focuses for the S- wave.

The aperture, over which we record the data that we back-propagate, is not perfect. This causes the spatial focuses, created using time reversal and deconvolution shown in Figures 2 and 3, to not be confined to one angular degree l because the spatial focuses are blurred in the z-direction. A perfect spatial focus would consist of only the $l = 1$ component. Figure 5 (a)-(b) and (c)-(d) shows cross sections of the backpropagated wavefields in Figures 2 and 3 in the x and z directions, respectively, so that it is easier to asses the improvements and comparisons between the two methods. Note that the scales of the horizontal axis for Figure 5 (a)-(b) are different from Figure 5 (c)-(d). Figure 5(a) demonstrates that

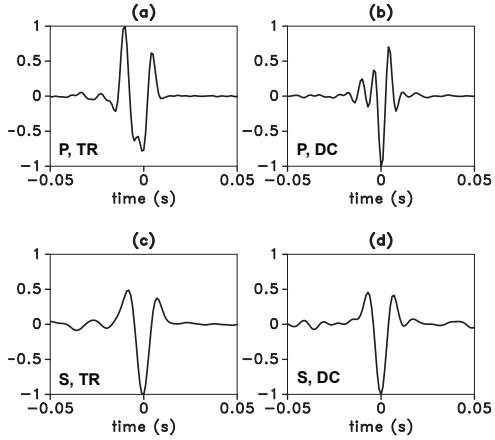

Figure 4. Temporal focused images due to a horizontal point force produced by back-propagating the calculated time reversed signals using time reversal and deconvolution for vertical borehole array. Part (a) and (b) are temporal focus of the P wave due to time reversal and deconvolution respectively. Part (c) and (d) are temporal focus of the S wave due to time reversal and deconvolution respectively.

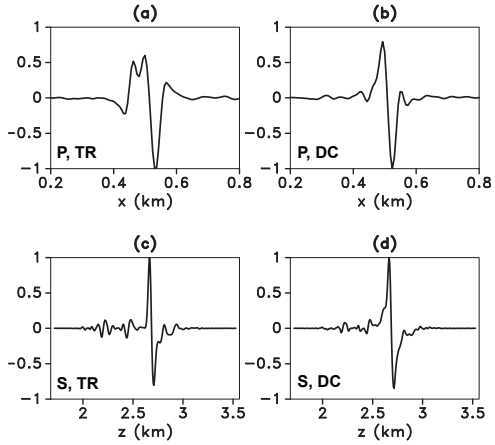

Figure 5. Spatial focused images due to a horizontal point force produced by back-propagating the calculated time reversed signals using time reversal and deconvolution. Part (a) and (b) are 1D slices of figure 2 through depth 2.68 km. Part (c) and (d) are 1D slices of figure 3 through x location .51km. Note the different scales used for the cross-section in the x and z direction.

time reversal is not able to create a well defined dipole focus in the x-direction which represents the radiation pattern of a P wave due to a horizontal point force. Figure 5(b) shows that deconvolution is able to reconstruct the dipole radiation pattern of the P wave due to a horizontal point force. Figure 5(c) and (d) demonstrate that there seems to be no significant difference between time reversal (c) and deconvolution (d) to reconstruct the S wave's rfocus.

Our numerical results have shown that deconvolu-

tion was able to improve the temporal focus for the P wave which led to an improved reconstruction of the P-wavefield's radiation pattern. However, deconvolution was not able to improve the temporal focus for the S-wave, due to a horizontal point force, which led to it also not improving the reconstruction of the S-wavefield's radiation pattern. This can be attributed to the fact that a nodal line for the S-wavefield's radiation pattern intersects the receiver array. Deconvolution will then apply a larger weight to the receivers near the nodal line in order to increase a weak recorded signal. This is unphysical because there is no information to be gained in these weak recorded waveforms near the nodal lines. These receivers are supposed to record no information about the source and should, therefore, not propagate any information back. However, it simultaneously demonstrates the robust nature of deconvolution. For the radiation pattern which has a nodal line intersecting the receiver array, deconvolution does not generate an inaccurate but rather a comparable reconstruction of the radiation pattern as time reversal.

We conclude that, for an elastic media without a perfect aperture and true velocity model, improved temporal focusing leads to improved spatial focusing. We have shown this both theoretically and numerically to be the case. Because deconvolution has the ability to improve the temporal focusing, one can improve the spatial focusing.

6 CONCLUSION

We have introduced deconvolution which improves the temporal focusing of microseismic events. We demonstrated theoretically and numerically that this improved temporal focusing leads to improved spatial focusing for each wave type in an elastic medium. This improved spatial focusing is beneficial for enhancing the focus of the elastic waves. The simplicity and robust nature of this method allows for a simple incorporation into existing reverse-time imaging methods. Additionally, the cost of deconvolution is minimal compared to running the finite difference modeling. Therefore, it can be added as a preprocessing step without significant additive cost.

7 ACKNOWLEDGMENT

We thank sponsor companies of the Consortium Project whose support made this research possible. The numerical examples in this paper use the madagascar package freely available at http://reproducibility.org/wiki/Main_Page.

REFERENCES

Aki, K., and P. Richards, 2002, Quantitative seismology, second ed.: Univ. Science Books.

Arfken, G., and H. Weber, 2001, Mathematical methods for physicists, 5th ed.: Harcourt.

Artman, B., I. Podladtchikov, and B. Witten, 2010, Source location using time-reverse imaging: Geophysical Prospecting, **58**, 861–873.

Aubry, J.-F., M. Tanter, J. Gerber, J.-L. Thomas, and M. Fink, 2001, Optimal focusing by spatio-temporal filter. II. Experiments. Application to focusing through absorbing and reverberating media: J. Acoust. Soc. Am., **110**, 48–58.

Bancroft, J., J. Wong, and L. Han, 2010, Sensitivity measurements for locating microseismic events: CSEG Recorder, 28–37.

Bertaix, V., J. Garson, N. Quieffin, S. Catheline, J. Derosny, and M. Fink, 2004, Time-reversal breaking of acoustic waves in a cavity: American Journal of Physics, **72**, 1308–1311.

Bose, S., H. Valero, Q. Liu, R. G. Shenoy, and A. Ounadjela, 2009, An Automatic Procedure to Detect Microseismic Events Embedded in High Noise: SEG Technical Program Expanded Abstracts, 1537–1541.

Chapman, C., 2004, Fundamentals of seismic wave propagation: Cambridge Univ. Press.

Douma, J., R. Snieder, A. Fish, P. Sava, and W. Phenomena, 2013, Locating a microseismic event using deconvolution: Proceedings of the 83rd Annual International Meeting, Society of Exploration Geophysicists., 2206–2211.

Duncan, P., 2005, Is there a future for passive seismic?: First Break, **23**, 111–115.

Fink, M., 1997, Time reversed acoustics: Physics Today, **50**, 34–40.

Fomel, S., 2007, Shaping regularization in geophysical-estimation problems: Geophysics, **72**, R29–R36.

Foulger, G., and B. R. Julian, 2012, Earthquakes and errors: Methods for industrial applications: Geophysics, **76**, WC5–WC15.

Gallot, T., S. Catheline, P. Roux, and M. Campillo, 2011, A passive inverse filter for Green's function retrieval: J. Acoust. Soc. Am., **131**, EL21–EL27.

Hayles, K., R. L. Horine, S. Checkles, J. P. Blangy, and H. Corporation, 2011, Comparison of microseismic results from the Bakken Formation processed by three different companies: Integration with surface seismic and pumping data: SEG Technical Program Expanded Abstracts, 1468–1472.

Jonsson, B. L. G., M. Gustafsson, V. H. Weston, and M. V. d. Hoop, 2004, Retrofocusing of acoustic wave fields by iterated time reversal: SIAM J. Appl. Math., **64**, 1954–1986.

Kendall, M., S. Maxwell, G. Foulger, L. Eisner, and Z. Lawrence, 2011, Special Section Microseismicity : Beyond dots in a box Introduction: Geophysics, **76**, WC1–WC33.

Kummerow, J., 2010, Using the value of the crosscorrelation coefficient to locate microseismic events: Geophysics, **75**, MA47–MA52.

Larmat, C., R. Guyer, and P. Johnson, 2010, Time-reversal methods in geophysics: Physics Today, **63**, 31–35.

Larmat, C., J. Montagner, M. Fink, Y. Capdeville, A. Tourin, and E. Clévédé, 2006, Time-reversal imaging of seismic sources and application to the great Sumatra eartquake: Geophys. Res. Lett., **33**, L19312, doi:10.1029/2006GL02636.

Lu, R., 2008, Time Reversed Acoustics and Applications to Earthquake Location and Salt Dome Flank Imaging: Massachusetts Institute of Technology. Earth Resources Laboratory.

Lu, R., N. Toksoz, and M. Willis, 2008, Locating Microseismic Events with Time Reversed Acoustics: A Synthetic Case Study: SEG Technical Program Expanded Abstracts, 1342–1346.

McMechan, G., J. Luetgert, and W. Mooney, 1985, Imaging of earthquake sources in Long Valley Caldera, California, 1983: Bull. Seismol. Soc. Am., **75**, 1005–1020.

Montaldo, G., M. Tanter, and M. Fink, 2004, Real time inverse filter focusing through iterative time reversal: J. Acoust. Soc. Am., **115**, 768–775.

Parvulescu, A., 1961, Signal detection in a multipath medium by M.E.S.S. processing: J. Acoust. Soc. Am., **33**, 1674–1674.

Roux, P., and M. Fink, 2000, Time reversal in a waveguide: study of the temporal and spatial focusing: J. Acoust. Soc. Am., **107**, 2418–2429.

Song, F., H. S. Kuleli, M. N. Toksöz, E. Ay, and H. Zhang, 2010, An improved method for hydrofracture-induced microseismic event detection and phase picking: Geophysics, **75**, A47–A52.

Steiner, B., E. H. Saenger, and S. M. Schmalholz, 2008, Time reverse modeling of low-frequency microtremors: Application to hydrocarbon reservoir localization: Geophysical Research Letters, **35**, L03307.

Tanter, M., J.-F. Aubry, J. Gerber, J.-L. Thomas, and M. Fink, 2001, Optimal focusing by spatio-temporal filter. I. Basic principles: J. Acoust. Soc. Am., **110**, 37–47.

Tanter, M., J.-L. Thomas, and M. Fink, 2000, Time reversal and the inverse filter: J. Acoust. Soc. Am., **108**, 223–234.

Ulrich, T., J. Douma, B. Anderson, and R. Snieder, currently under review, 2013, Improving spatio-temporal focusing and source reconstruction through deconvolution: Wave Motion.

Vignon, F., J.-F. Aubry, A. Saez, M. Tanter, D. Cassereau, G. Montaldo, and M. Fink, 2006, The Stokes relations linking time reversal and the inverse filter: J. Acoust. Soc. Am., **119**, 1335–1346.

Wu, R.S.and Ben-Menahem, A., 1985, The elastodynamic near field: Geophys. J.R. Astron. Soc., **81**, 609–622.